═══════════ REVIEW ═══════════

Optical Methods for Formation of Radiation Patterns of Phased Array Antennas

R. B. Vaganov[†], I. P. Korshunov, E. N. Korshunova, A. D. Oleinikov, and A. D. Shatrov

*Kotel'nikov Institute of Radio Engineering and Electronics (Fryazino Branch), Russian Academy of Sciences,
pl. Vvedenskogo 1, Fryazino, Moscow oblast, 141190 Russia
e-mail: korip@ms.ire.rssi.ru*

Received May 11, 2012

Abstract—It is shown that architectural design principles based on application of photonics methods have prospects for the development of ultra-wideband and ultrashort-pulse radars. Transmitting and receiving systems with optical controllers based on dispersing fiber-optic prisms are considered. Design versions of a photoconductive antenna excited by picosecond optical pulses and a wideband photoelectronic pattern shaper on the basis of analog vector modulation are presented. A method for compensation of antenna distortion effects arising during transmission of an ultrashort pulse with the use of an optical shaping technique is described.

INTRODUCTION

Exacting requirements on the accuracy of determination of objects' spatial coordinates as well as spatial angular resolution of radar images initiated development of ultra-wideband (UWB) and ultrashort-pulse (USP) radar. In most designs of UWB and USP radars, preference is given to systems with phased array antennas (PAAs) (with numbers of elements of 10^3–10^4). This preference drastically changes not only the architecture of such radars but also the design principles of their main functional parts and components. In this review, we analyze architectural designs of UWB and USP radars based on application of optical and optoelectronic methods.

Optoelectronic methods and means (which are usually called photonics) [1, 2] used for formation of the radiation pattern and its real-time azimuth and elevation scanning have several incontestable advantages over traditional electromechanical methods in mass, overall dimensions, noise immunity, operation speed, etc. In modern UWB radars, formation and control of the PAA radiation pattern is ensured by fast photoelectronic controllers, which have such important advantages as unification of functional parts and applicability and integrated optical technologies for manufacturing of matrices of semiconductor lasers, electrooptical modulators, photoreceivers, phase shifters, and integrated packages of wideband microwave amplifiers.

Special photoelectronic controllers can be used for the real-time synthesis of required waveforms of radiated pulsed signals that are matched to receiving and transmitting antennas. This excludes appearance of the so-called antenna distortion (dispersion spreading of the pulse). Moreover, applying integrated optical technologies, one can substantially improve the reliability of operation of the entire system. The effect of photoinduced microwave radiation, which is generated by special doped films illuminated by high-power optical pulses, can be used for construction of a compact feed of reflector antennas.

1. MASTER CONTROLLER BASED ON DISPERSING FIBER-OPTIC PRISMS

In this section, we consider the design and principle of operation of transmitting and receiving PAAs in which the radiation pattern is formed and controlled by a controller based on fiber-optic dispersing prisms (FODPs).

1.1. Two-Dimensional Transmitting PAA

The transmitting PAA is an array formed by 4 × 4 radiating elements operating in the frequency band 6–18 GHz in the chirp mode. The array ensures azimuth and elevation scanning in an angular interval of ±30° [3]. The functional block diagram of the experimental prototype of the transmitting PAA is shown in Fig. 1, where optical links are shown by solid lines and electric links, by dashed lines. Almost all units of the prototype operate on optical carriers, except for the output stages of the PAA where chirp signals are extracted and fed to the radiating antenna elements.

The analyzed system consists of two units having identical design and structure: the azimuth unit and the elevation unit. Each of these units receives optical
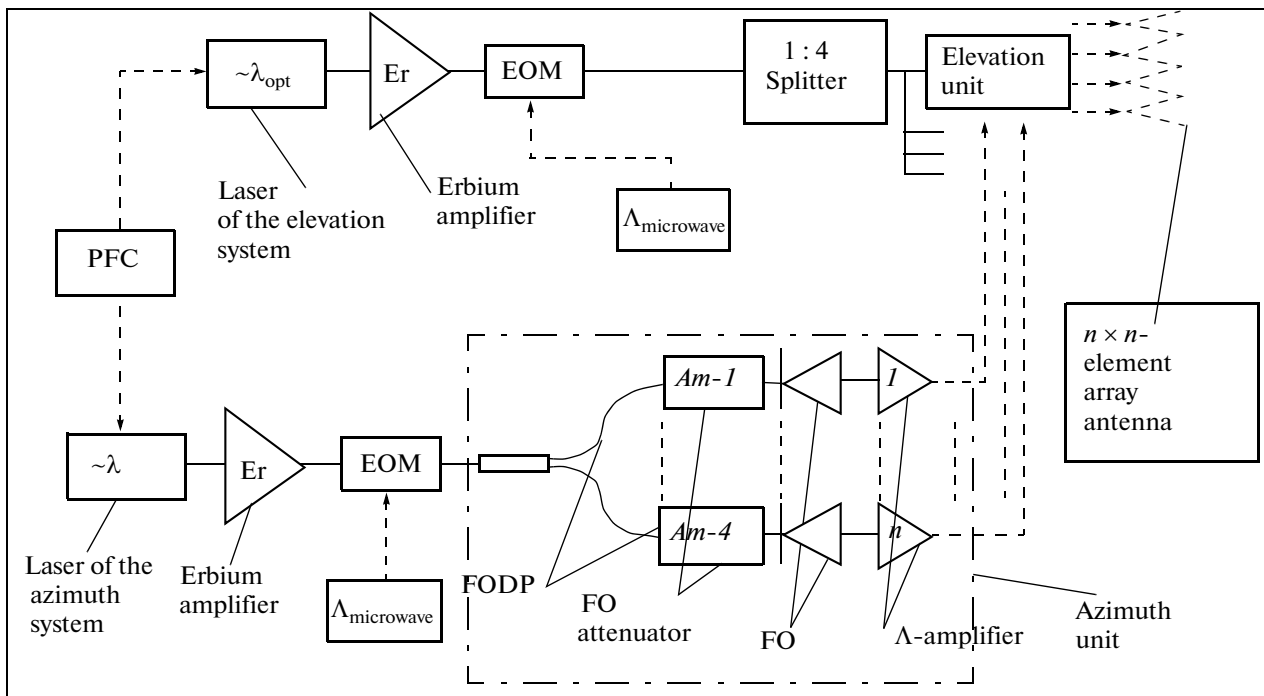
[†] Deceased.

Fig. 1. Functional block diagram of the transmitting UWB array on the basis of fiber-optic dispersing prisms.

beams from autonomous lasers whose radiation is preliminary amplified by corresponding erbium amplifiers. Azimuth and elevation scanning intervals are controlled by a programmable frequency control (PFC) unit, which varies the wavelengths radiates by corresponding lasers. Optical beams formed at the outputs of erbium amplifiers enter wideband microwave electrooptical modulators (EOMs) excited by corresponding chirp signals. Then, optical carriers in the azimuth and elevation units are separated into $n = 4$ channels (where n is the number of elements in the rows and columns of the PAA) and enter the FODP inputs.

Fiber-optic dispersing prisms are manufactured from a single-mode fiber with high group dispersion of the refractive index $D = 88$ ps/(nm km). The prisms ensure the required value of the phase delay of the microwave subcarrier (Λ) in each individual circuit of the PAA, which is proportional to the number of the corresponding row and/or column of the antenna element in the array. Detuning $\Delta\lambda$ of the optical wavelength required for the specified value of optically controlled angle θ_0 is determined by the expression

$$\Delta\lambda = \frac{d\sin(\theta_0)}{cDl}, \tag{1}$$

where d is the spacing (discrete) between the antenna elements of the PAA, l is the length of a particular fiber circuit, and c is the velocity of light in vacuum. A FODP tuning and calibration technique was considered in [4]. In order to ensure the required values of the azimuth and elevation pattern scanning intervals ($\pm30°$), laser generation wavelengths are varied from

1525 nm to 1545 nm. Each fiber-optic (FO) circuit contains FO attenuator $Am - i$ ($i \in 1-4$), which ensures frequency independence of the transmission coefficient at the microwave subcarrier. Modulated optical carriers formed at the outputs of each channel attenuator $Am - i$ enter microwave photodetectors ($p-i-n$ photodiodes). Their output microwave signals then pass through channel microwave amplifiers (with a gain of ~39 dB) and enter corresponding radiating elements of the PAA.

Amplitude–frequency characteristics (AFCs) and phase–frequency characteristics (PFCs) measured for the signals arriving from the controller at the PAA radiating elements are shown in Figs. 2 and 3, respectively. The values of rms deviations of transmission coefficient $\Gamma(f)$ and phase fluctuations $\Phi(f)$ in an ensemble of 16 forming circuits at low and moderately high frequencies are ±1 dB for the transmission coefficient and $\pm5°$ for the phase.

Pulsed responses of the system calculated from the AFCs and PFCs measured in different operating conditions are shown in Fig. 4. Curve *1* corresponds to the case of $\Delta\lambda_{az} = 0$ and $\Delta\lambda_{el} = 0$, when the PAA radiates in the direction perpendicular to its plane. In this case, signals of the microwave subcarriers of all PAA elements are summed with the same phase and the pulsed response obtained by means of the inverse Fourier transform of the complex AFC is a monopulse with zero time delay. Curve *2* was obtained for $\Delta\lambda_{az} = 28$ nm and $\Delta\lambda_{el} = 0$. In this case, signals of the microwave subcarrier of each column of the PAA element are summed with the same phase and four PAA elements
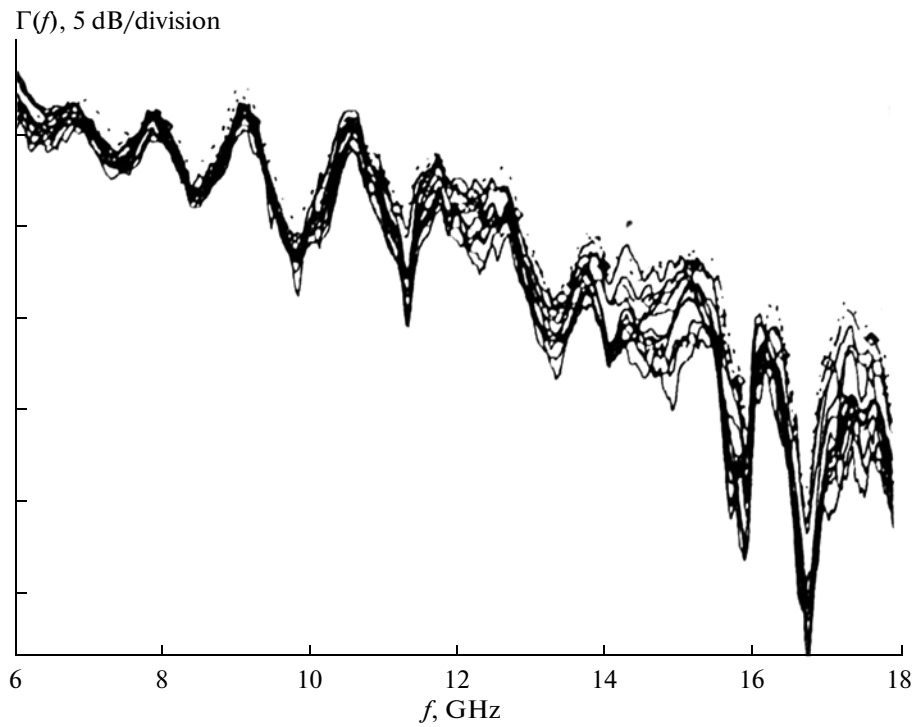
Γ(*f*), 5 dB/division

Fig. 2. Amplitude−frequency characteristics of the signals entering 16 radiating elements of the experimental PAA.

Φ(*f*), deg

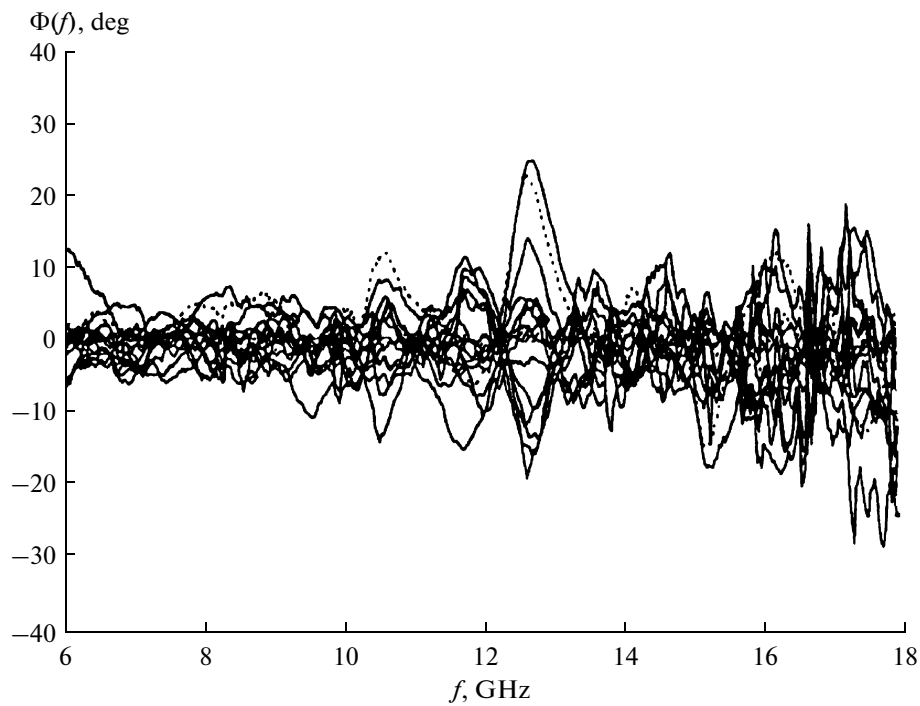**Fig. 3.** Phase−frequency characteristics of the signals entering 16 radiating elements of the experimental PAA.
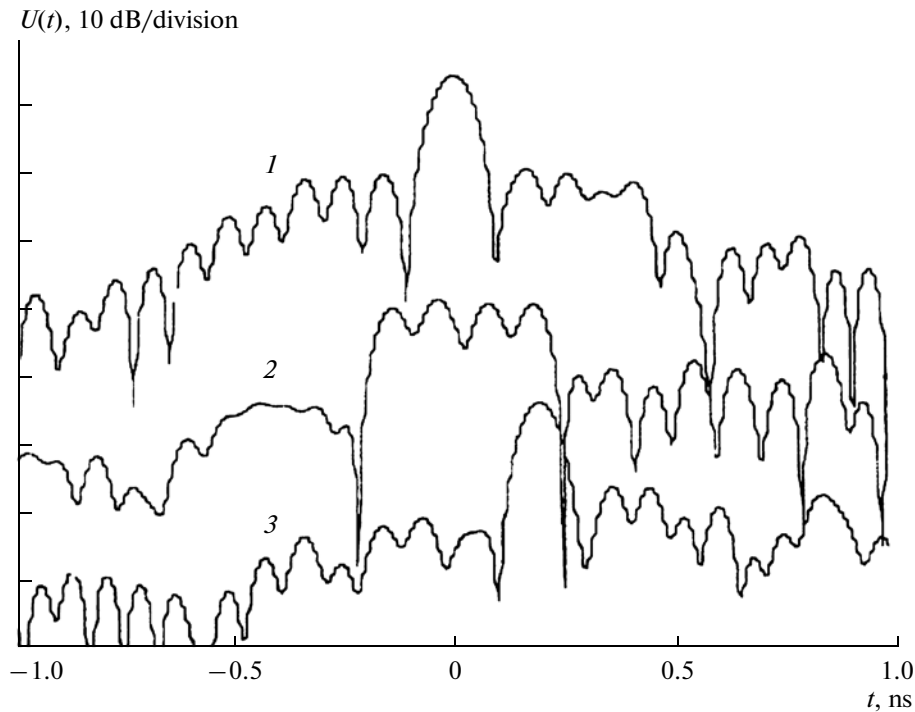
$U(t)$, 10 dB/division

Fig. 4. Array pulsed responses (retrieved from the AFC and PFC) for different phasing methods: (*1*) $\Delta\lambda_{az} = 0$ and $\Delta\lambda_{el} = 0$, (*2*) $\Delta\lambda_{az} = 28$ nm and $\Delta\lambda_{el} = 0$, and (*3*) $\Delta\lambda_{az} = 28$ nm and $\Delta\lambda_{el} = 24.5$ nm.

situated in a row radiate fields with their phase shifts ($\Delta\lambda_{az} = 28$ nm); as a result, a four-lobe pulsed response with a pulse interval of ~500 ps is formed. Curve *3* corresponds to the case of $\Delta\lambda_{az} = 28$ nm and $\Delta\lambda_{el} = 24.5$ nm, when the PAA radiates at an angle of $-60°$. In this case, signals of the microwave subcarrier of each of 16 PAA elements are summed with their phase shifts, which results in formation of a multipulsed response with a pulse interval of ~110 ps.

1.2. One-Dimensional Receiving PAA

The analyzed receiving PAA is formed by eight wideband spiral antennas arranged into a linear array antenna. The frequency band ensured by these elements is 2−18 GHz [5]. The functional block diagram of the experimental prototype of the receiving PAA is shown in Fig. 5. In each of $n = 8$ channels of this prototype, phase delays are controlled by a controller similar to that described in the preceding section. Microwave signals received by each spiral antenna enter inputs of 40-dB microwave amplifiers and, then, microwave inputs of electrooptical modulators. Optical inputs of these EOMs are fed with optical radiation from a laser with tunable frequency. This radiation is preliminary amplified by an erbium amplifier and is separated into eight channels by a multiplexer. The frequency of the radiation generated by the laser is varied from 1535 nm to 1565 nm by a frequency control unit (FCU). Low-noise microwave amplifiers used in the PAA have a gain of ~40 dB ± 2 dB in the frequency

band 6−18 GHz and ensure a nonlinearity of the phase characteristic of no more than ±10°. The optical output of each channel EOM is connected to a FODP, which ensures the phase shift of the microwave subcarrier corresponding to the number of each antenna element and the specified value of the pattern's azimuth scanning angle. Radiations from the outputs of all eight FODPs are combined by a FO multiplexer into one channel and a fed to a photodiode. Since output radiations of eight FODPs correspond to different wavelengths, the photodetector combines intensities rather than optical fields. If phase delays created by all FODPs are the same, the so-called intensity interference effect appears. The microwave signal from the photodiode output enters a 40-dB amplifier and then is used for recording.

The results of measuring the characteristics of the experimental prototype of the linear PAA in an anechoic chamber are presented in Figs. 6 and 7. Amplitude−frequency characteristics $U(f)$ and phase−frequency characteristics $\Phi(f)$ of all eight channels for a fixed pattern scan angle of $-60°$ (corresponding to $\lambda = 1535$ nm and $\Delta\lambda = -15$ nm) are shown in Fig. 6. The shapes of the PAA pulsed responses calculated from the AFCs and PFCs measured in different scanning conditions are shown in Fig. 7. Curve *1* corresponds to the case of $\Delta\lambda = 0$, when the PAA radiates in the direction perpendicular to its plane. In this case, signals of the microwave subcarriers of all PAA elements are summed with the same phase and the pulsed
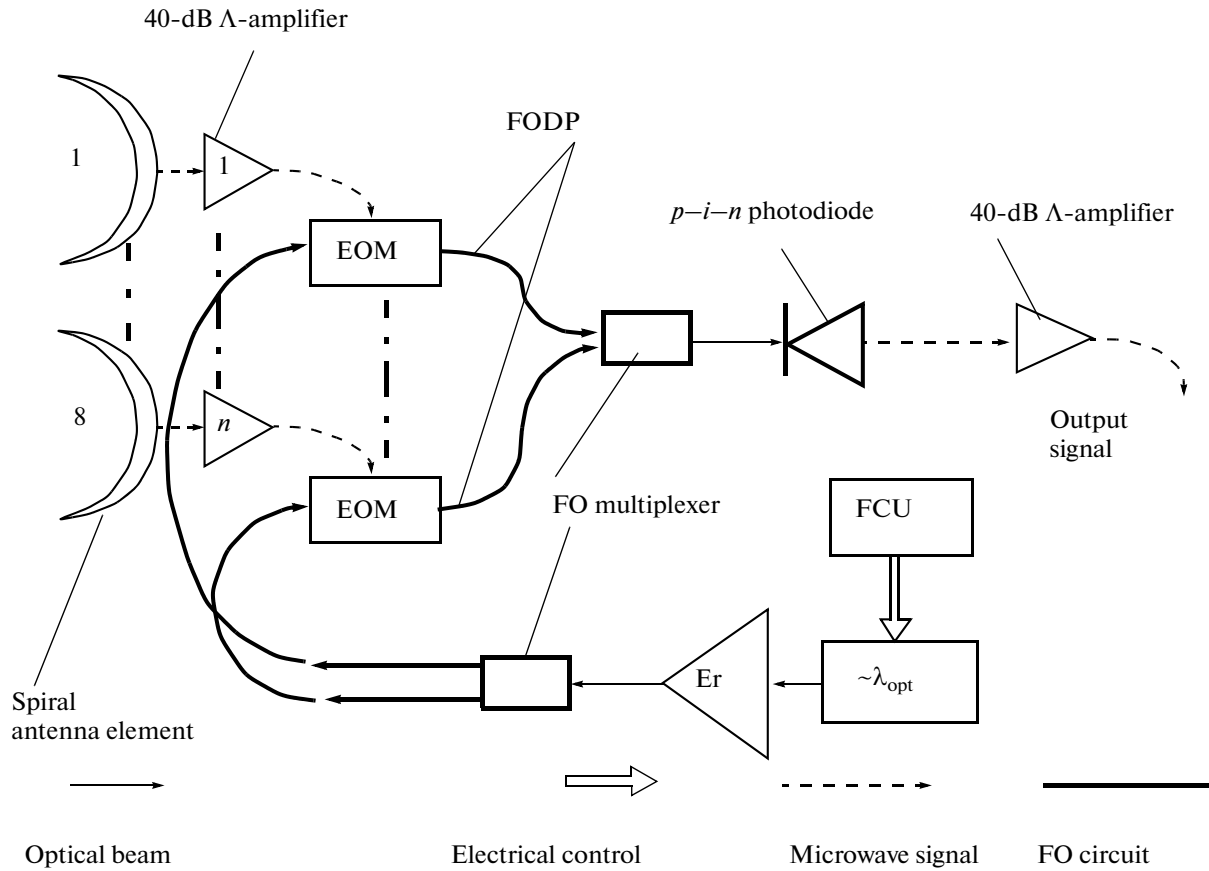
Fig. 5. Functional block diagram of the eight-element receiving PAA with a master controller on the basis of FODP.
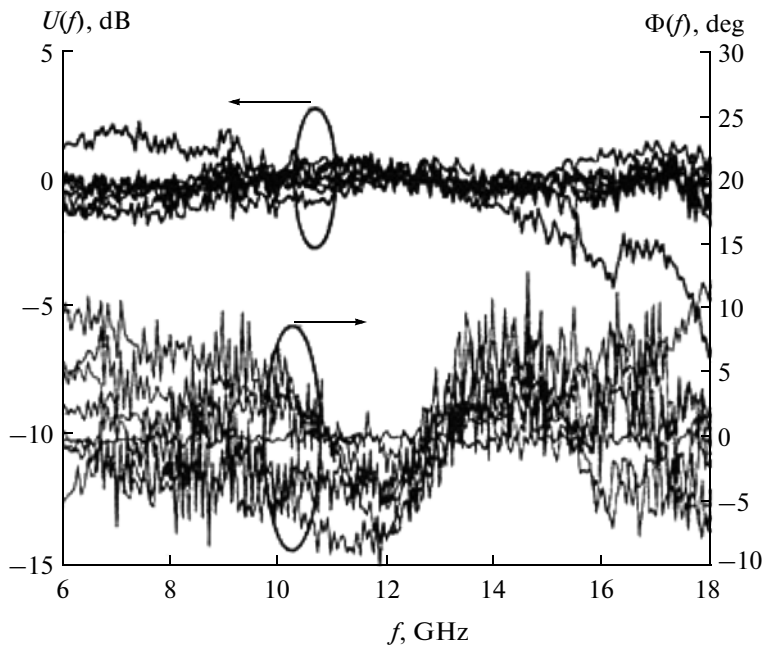

Fig. 6. Amplitude and phase characteristics of eight channels of the receiving PAA with a master controller on the basis of FODP.
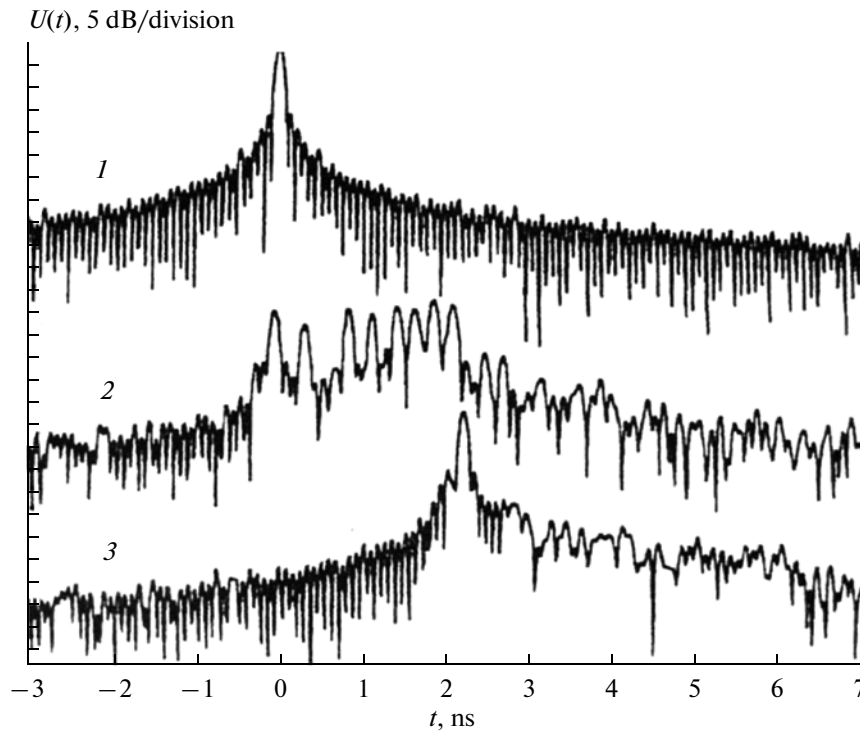
U(t), 5 dB/division

Fig. 7. Pulsed responses synthesized from the amplitude and phase characteristics of the eight-channel receiving PAA for different pattern scanning modes: (*1*) $\Delta\lambda = 0$ and $\varphi = 90°$, (*2*) $\Delta\lambda = 0$ and $\varphi = -60°$, and (*3*) $\Delta\lambda = -15$ nm and $\varphi = -60°$.

response obtained by means of the inverse Fourier transform of the complex AFC is a monopulse. Curve *2* was obtained for $\Delta\lambda = 0$, but the PAA radiates at an angle of $-60°$. In this case, signals of the microwave subcarriers of all PAA elements are summed with their phase shifts, which results in formation of an eight-lobe pulsed response. Curve *3* corresponds to $\Delta\lambda = -15$ nm in the case when the PAA is radiated at an angle of $-60°$. Here, signals of the microwave subcarriers of all PAA elements are summed with the same phase but with an angular shift of $-60°$, which corresponds to a delay of 2 ns of the pulsed response.

2. PLANAR PHOTOCONDUCTING ANTENNA EXCITED BY PICOSECOND OPTICAL PULSES

Photoconducting antennas excited by short laser pulses can serve as efficient sources of wideband electromagnetic radiation in UWB radars. In radar technology, a photoconducting antenna operating in the gigahertz band may be preferable than in the terahertz band due to its better absorbing and scattering characteristics. It has been shown in [6] that illumination of an In:Fe film by picosecond optical pulses causes generation of microwave pulses with an equivalent frequency band of 1−20 GHz.

The layout of the experimental setup is shown in Fig. 8. Mode-locked laser YLF with switched Q factor generates 50-ps pulses with an energy of 30 μJ at a

wavelength of 527 nm. A Pockels cell is used for time-ranking the laser pulses in the pulse selector at a frequency of 400 Hz. Then, a beam splitter is used to split the laser beam into two parts, one of which ensures locking of a high-speed oscilloscope with the help of a wideband photodetector. The main beam passes through a 15-m-long optical delay line formed by five mirrors, which ensures an interval of recorded frequencies of about 40 GHz. Upon passing through the delay line, the optical beam is collimated by an optical system and is directed to an In:Fe film with high value of the dark resistance ($>10^8$ Ω). A transient photocurrent, which becomes the source of wideband microwave radiation, is generated in the photoconducting film.

A typical waveform of the signal received from a distance of 3 m at a low-energy level of the optical excitation of the film (<10 μJ/cm^2) is shown in Fig. 9 as a function of delay time τ. In this case, the receiver is a special UWB photodetector, which records pulses with duration of about 50 ps. The shape of these pulses almost coincides with the shape of laser pulses.

The relationship between surface photoconductivity σ_S and intensity of optical radiation I_{opt} can be represented as follows [7]:

$$\sigma_S(t) = \frac{e\mu(1-R)}{h\nu} \int_{-\infty}^{t} dt' I_{opt}(t') \exp\left[\frac{(t-t')}{\tau_r}\right], \qquad (2)$$

where e is the electron charge, μ is the carrier mobility in the photoconductor, R is the optical reflection coef-
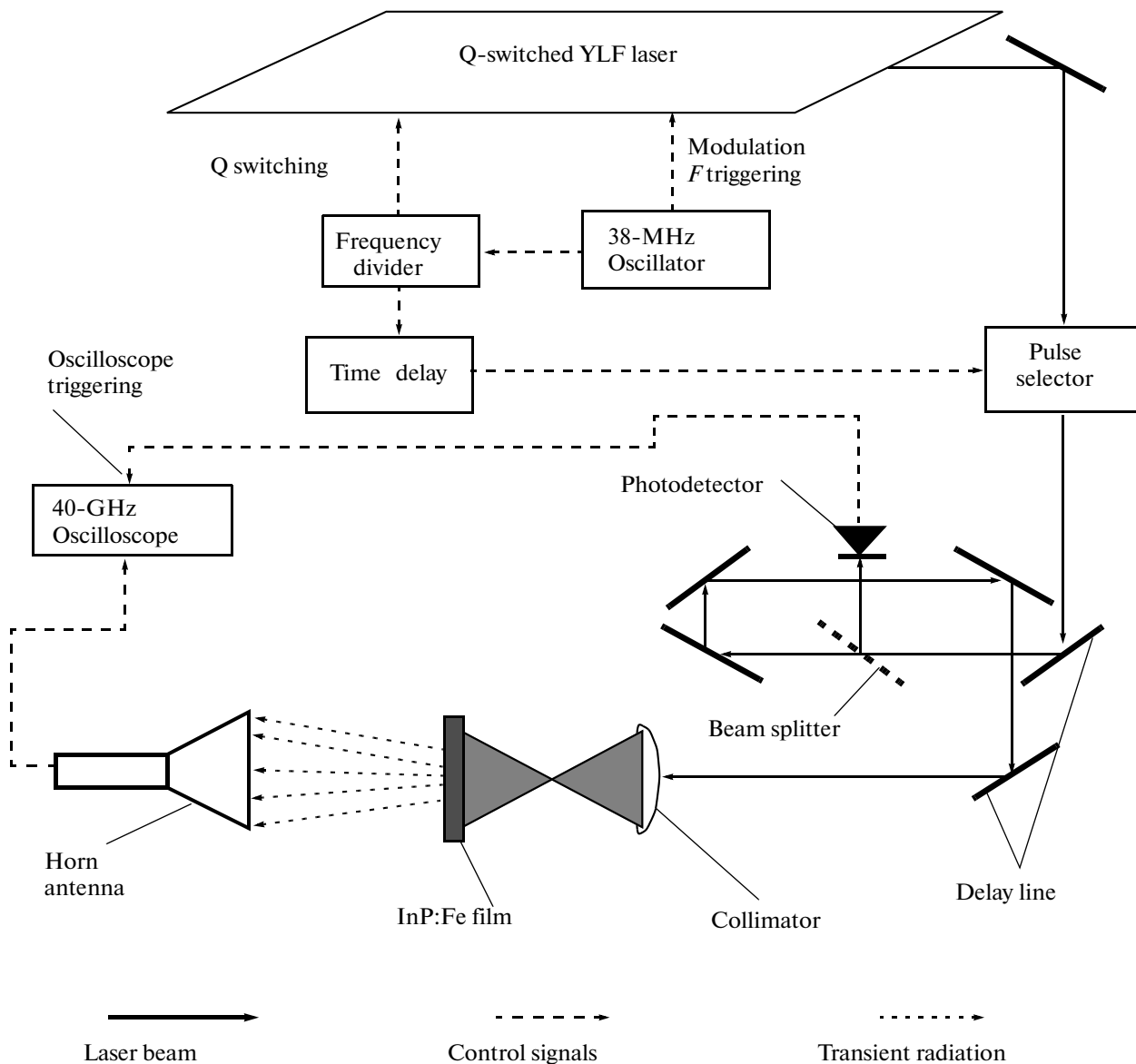
Fig. 8. Functional block diagram of the experimental setup for illustration of operation of the photoconducting radiating antenna.

ficient, $h\nu$ is the photon energy, and τ_r is the photon lifetime (it is known that $\tau_r \geqslant 50$ ps). It follows from (2) that, at low levels of optical excitation, the radiated field is proportional to the optical intensity. The strong saturation effect appears when the density of the optical flow exceeds 100 μJ/cm^2 (see Fig. 10). In addition, in this case, the radiation waveform changes from almost a half-period to a full wave.

The radiation of the photoconducting film recorded in the far zone with the help of a horn antenna with a ridge-waveguide converter is shown in Fig. 11. It can be readily noticed that the waveform of received radiation corresponds to the first derivative of the photocurrent in the film. The phase of the microwave radiation can be efficiently modulated with the

use of optical methods This fact is illustrated in Fig. 12 depicting recorded waveforms of two different fiber radiation sources. Curves *1* and *3*, which are shifted along the horizontal axis, correspond to illumination by isolated sources and curve *2* corresponds to simultaneous illumination by two sources. Tuning of the optical path difference in two fiber sources is equivalent to a mutual phase shift of microwave signals induced by these sources.

Coherent nature of the radiation induced by one InP:Fe film can be used to develop a PAA in the gigahertz wave band, which can be used, for example, as a feed of a parabolic reflector antenna. Let us analyze the energy properties of such a feed. One element of an InP:Fe film with a thickness of absorbing layer of 1 μm
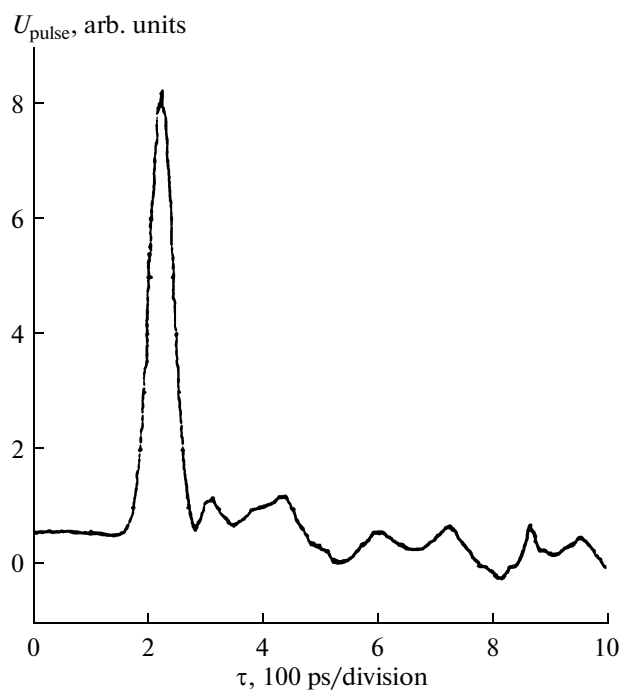
Fig. 9. Electromagnetic pulse generated by the In:Fe film illuminated by a 50-ps laser pulse.
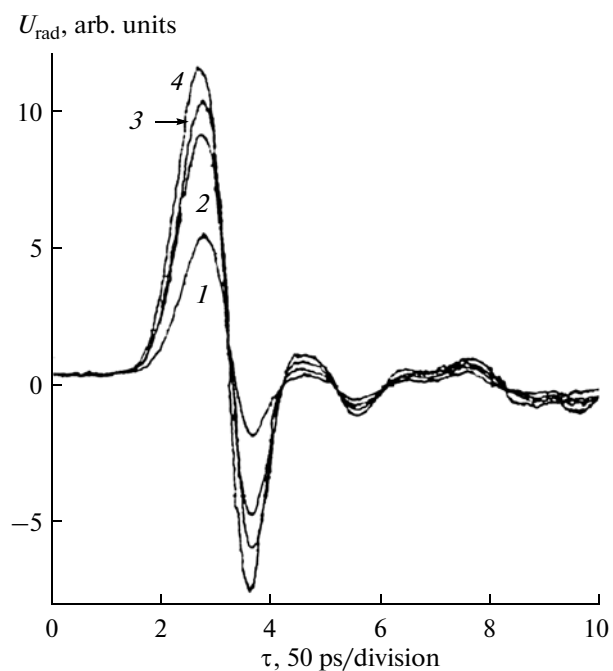

Fig. 10. Waveforms generated by the In:Fe film illuminated by a 50-ps laser pulse for different densities of optical power I_{opt}. Curves *1–4* correspond to $I_{opt} = 25, 83, 125,$ and 250 μJ/cm^2, respectively.
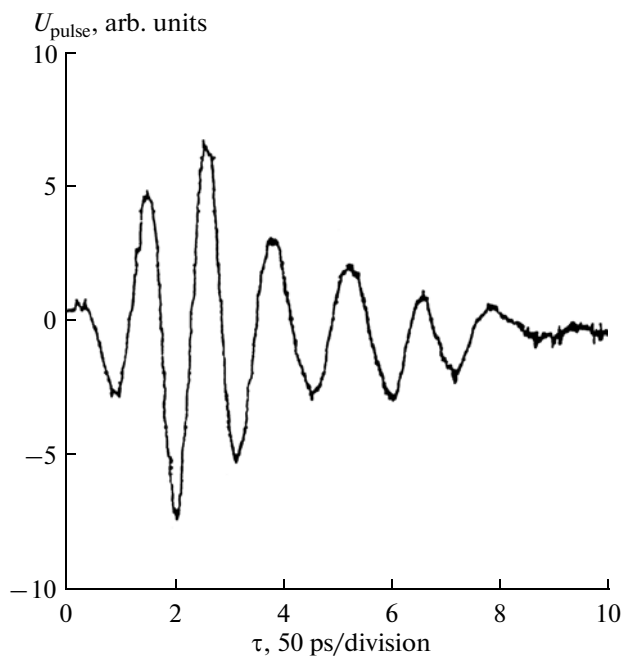

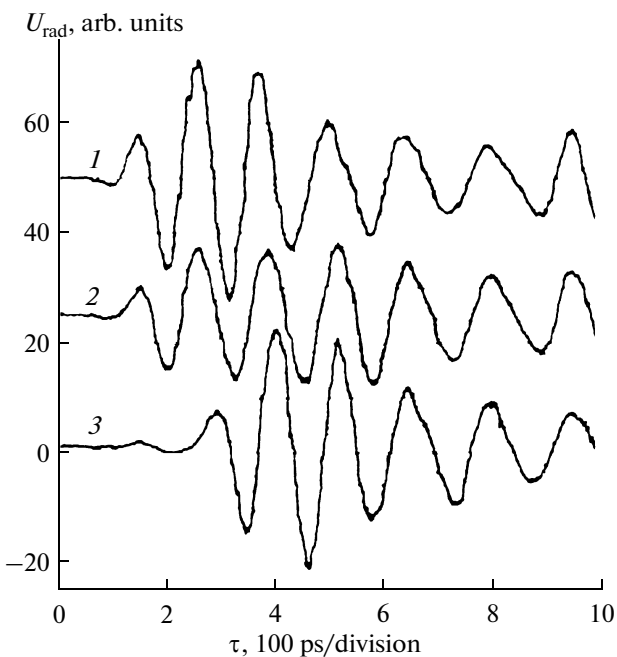**Fig. 11.** Microwave output signal received by the *K*-band ridged waveguide converter.

Fig. 12. Radiated waveforms induced by different sources of optical radiation: curves *1* and *3* correspond to isolated feeds and curve *2* corresponds to two fiber sources.

ensures conversion of the static electric energy accumulated on the film surface with an area of 10 cm² during 50 ps into the radiation with a peak power of 1 kW. Then, a radiator in the form of an array of 10×10 film elements ensures a total power of 100 kW in a pulse with a duration of 50 ps. Transverse dimensions of such a radiator are about 30×30 cm².

3. WIDEBAND PHOTOELECTRONIC PATTERN SHAPER BASED ON ANALOG VECTOR MODULATION

A new principle of the photoelectronic control of the phase of array antennas, which is fee of direct dependence on optical phase shifts requited for formation of equivalent shifts of the RF subcarrier on array elements, was considered in [8, 9]. This photoelectronic controller uses analog vector phase modulation of signals. The block diagram explaining the algorithm of formation of phase shifts in the interval $0°–360°$ for the RF signal is shown in Fig. 13. An important point in implementation of the inphase–quadrature method is the weighted summation of two phase-shifted quadrature copies of the signal in which the relative weight of summed signals controls the amplitude and phase of the resulting vector signal.

The system input is fed with RF signal $c(t)\sin(\omega t)$, which is used to form sine and cosine components. Then, these components are branched into four channels, each adding a fixed phase shift $\Delta\varphi$ ensuring covering of four quadrants in the interval $0°–360°$. Each channel contains two microwave amplifiers. Their gains are adjusted so that the condition $V \equiv$ const is fulfilled for any specified value of angular phase shift θ.

In each of four channels, output signals of these amplifiers enter channel combiners Σ. The combiners ensure vector summation, i.e., formation of output control signals with amplitude $Vc(t)$ and current phase $(\omega t \pm \theta)$. Control of the RF signal phase in the interval $0°–360°$ requires application of two pairs of amplitude tuning circuits. In the considered controller, these amplitude-control operations can be ensured by three nematic liquid-crystal optical modulators (LCOMs).

The functional block diagram of one design version of a photoelectronic controller using the algorithm described above is shown in Fig. 14. The signal from a microwave oscillator passes through the circuit of an inphase–quadrature vector shaper and enters two injection lasers operating at a wavelength of 1310 nm. The frequency bandwidth of the circuits of the inphase–quadrature vector shaper is $1–2$ GHz. The modulated laser radiation passes through FO lines and enters two autonomous channels. One of these channels extracts the *s*-polarized component of light and the other, the *p*-polarized component. The polarized components are extracted by properly oriented polarization analyzers. The components of light transmitted through the analyzers enter two autonomous controllable single-pixel spatial modulators, LCOM-1

and LCOM-2. The experimental setup contains LCOMs ensuring a resolution of 1 : 5000 in the range of controlled transmission of corresponding polarized components of light.

Orthogonally polarized components of light transmitted through LCOM-1 and LCOM-2 are reduced in accordance with the controller commands and enter an optical combiner designed as a beam-splitting cube. Since the electric lengths of FO circuits transmitting the laser light are balanced on the scale of the wavelength of the microwave subcarrier, the beam whose intensity equals the sum of intensities of combined orthogonally polarized components of light is formed at the output of the optical combiner. The electric signal at the output of the photodiode is proportional to the intensity of the detected optical flow. In this case, the amplitude and phase of the signal of the microwave subcarrier are, respectively,

$$V_\theta = Q\sqrt{K_s^2 + K_p^2},$$
$$\theta = \arctan\frac{K_s}{K_p}, \tag{3}$$

where Q is the proportionality coefficient and K_s and K_p are the intensity transmission coefficients of LCOM-1 and LCOM-2, respectively. Studies of the experimental prototype of vector controller at a frequency of 1017 MHz confirmed the linearity of the phase shift in the interval $0°–360°$.

The considered method for construction of the optical controller for control of microwave PAAs has several advantages over other methods: in this controller, optical interference effects are almost eliminated and a limited number of bulk electrooptical components (four lasers, microwave electrooptical modulators, and optical combiners) is used. It should be noted that a technique for manufacturing LCOMs in the form of arrays consisting of 1500 elements controlled by a built-in electronic controller has already been tested.

4. COMPENSATION OF ANTENNA DISTORTION EFFECTS DURING TRANSMISSION OF ULTRASHORT PULSES WITH THE HELP OF AN OPTICAL SHAPING TECHNIQUE

Application of photonic methods is especially promising for not only formation of radiation patterns and control of UWB PAAs but also compensation of signal distortion arising during radiation and reception of USPs. In recent years, theoretical studies [10, 11] on optimization of pulsed waveforms ensuring compensation of PFC distortions appeared. Such an optimization was implemented in [11] using the method of generation of arbitrary waveforms, including those preliminary compensated with respect to the antenna distortion. While measurements were performed in
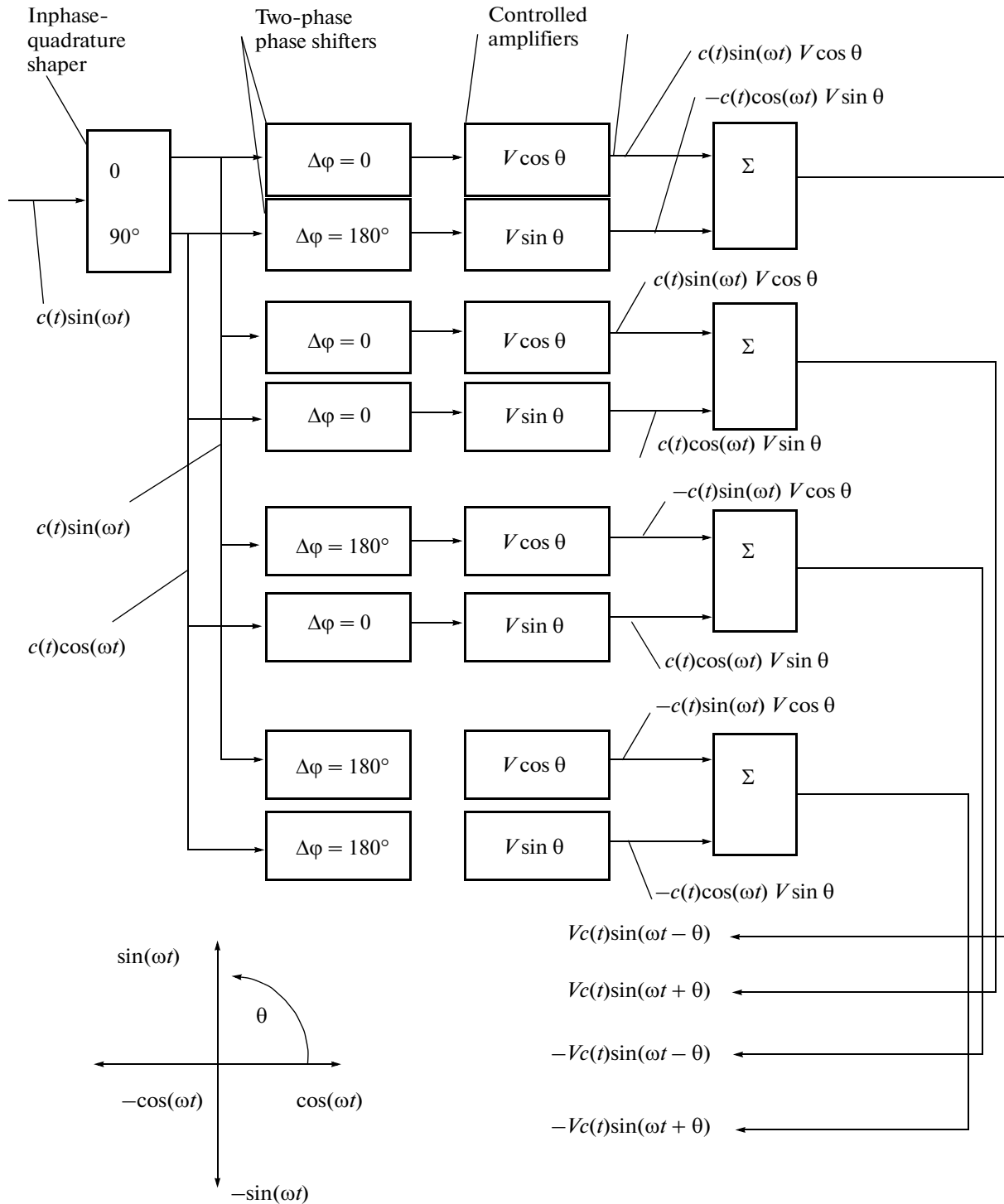
Inphase-
quadrature
shaper

Two-phase
phase shifters

Controlled
amplifiers

$c(t)\sin(\omega t)\,V\cos\theta$

$-c(t)\cos(\omega t)\,V\sin\theta$

| 0 |
| 90° |

| $\Delta\varphi = 0$ | $V\cos\theta$ | Σ |
| $\Delta\varphi = 180°$ | $V\sin\theta$ | |

$c(t)\sin(\omega t)$

$c(t)\sin(\omega t)\,V\cos\theta$

| $\Delta\varphi = 0$ | $V\cos\theta$ | Σ |
| $\Delta\varphi = 0$ | $V\sin\theta$ | |

$c(t)\cos(\omega t)\,V\sin\theta$

$c(t)\sin(\omega t)$

$c(t)\cos(\omega t)$

$-c(t)\sin(\omega t)\,V\cos\theta$

| $\Delta\varphi = 180°$ | $V\cos\theta$ | Σ |
| $\Delta\varphi = 0$ | $V\sin\theta$ | |

$c(t)\cos(\omega t)\,V\sin\theta$

$-c(t)\sin(\omega t)\,V\cos\theta$

| $\Delta\varphi = 180°$ | $V\cos\theta$ | Σ |
| $\Delta\varphi = 180°$ | $V\sin\theta$ | |

$-c(t)\cos(\omega t)\,V\sin\theta$

$Vc(t)\sin(\omega t - \theta)$

$Vc(t)\sin(\omega t + \theta)$

$-Vc(t)\sin(\omega t - \theta)$

$-Vc(t)\sin(\omega t + \theta)$

$\sin(\omega t)$

θ

$-\cos(\omega t)$

$\cos(\omega t)$

$-\sin(\omega t)$

Fig. 13. Algorithm for formation of phase shifts in the interval $0°-360°$ for the RF signal.

time domain, the possibility of retrieval of the infor-
mation on distortions of the RF PFC introduced into
the transmitted signal by transmitting and receiving
horn antennas was demonstrated. This allows one to
introduce the conjugate spectral phase into the trans-
mitted waveform and thus ensure time compression of
the pulse in the receiver.

4.1. Principle of Formation
of Specified Electromagnetic Waveforms

The functional block diagram of the experimental
setup for studying the possibility of compensation of
antenna distortions is shown in Fig. 15. Radiating and
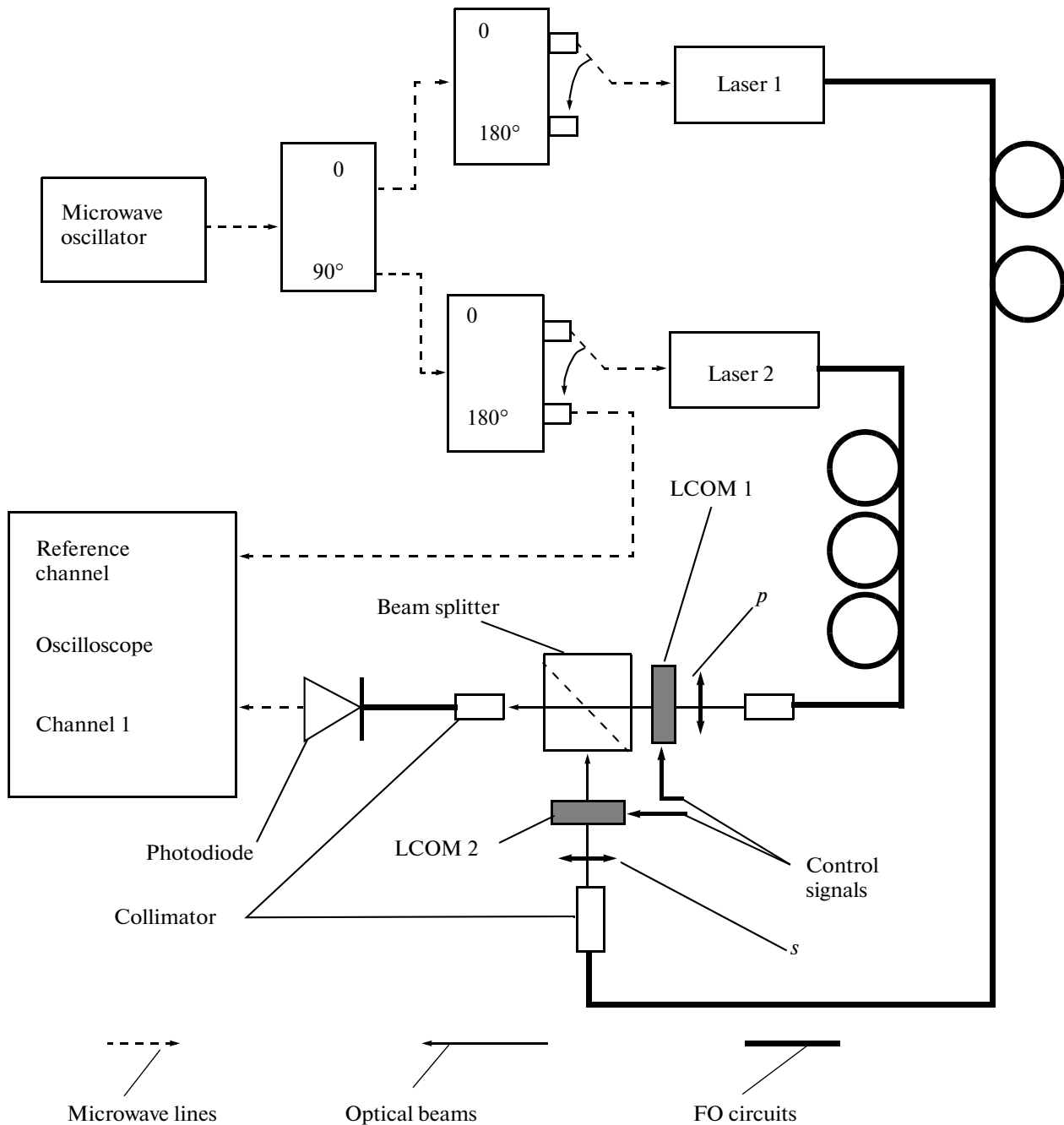receiving antennas are ridged horns ensuring opera-

Fig. 14. Functional block diagram of the experimental setup for demonstration of analog vector control of the RF-signal phase.

tion in the frequency band 1−12 GHz. The output signal formed by the waveform synthesis unit (WSU) is amplified by a wideband amplifier and is fed to the radiating horn antenna. The output signal of the receiving antenna, which is practically located in the far zone, is recorded by a 50-GHz oscilloscope.

The considered system uses synthesis of the required waveform with the help of a fast optical shaper [12]. Femtosecond pulses from an erbium fiber-optic laser enter the input of the WSU. Spectra of optical pulses with a duration of 100 fs and a repetition frequency of 50 MHz are filtered in a Fourier shaper.

During propagation in a single-mode optical fiber with a length of 5.5 km, short optical pulses disperse. The chromatic dispersion of this fiber uniquely ranks the corresponding frequencies on the time scale.
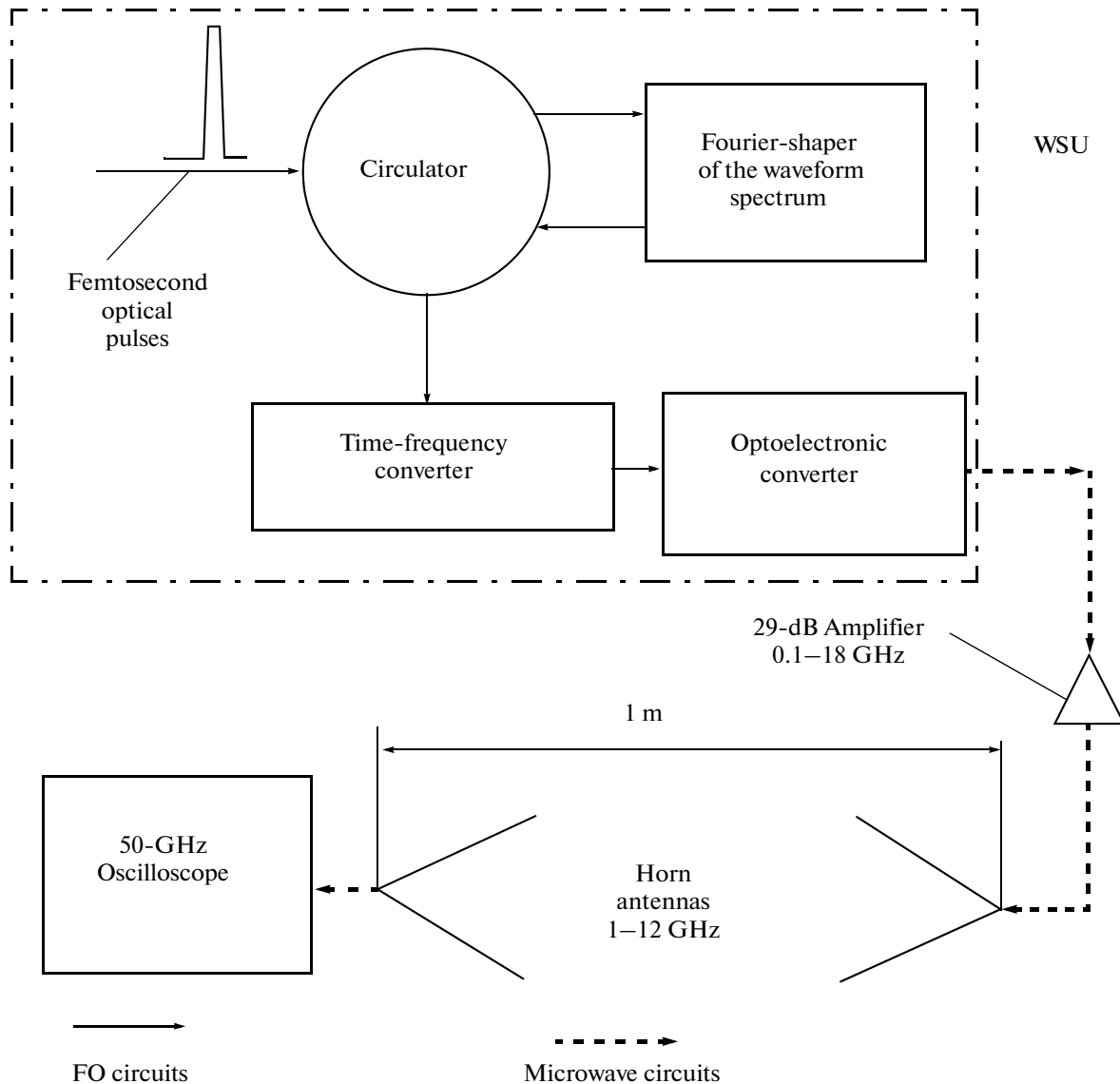
Fig. 15. Functional block diagram of the photoelectronic device forming optimum waveforms for compensation of the antenna distortion.

Thus, the time-domain distribution of the optical intensity at the output of the fiber-optic circuit is a scaled image of the filtering function corresponding to the given waveform. Then, these formed optical waveforms are converted by an optoelectronic converter into an electric signal with the help of a 60-GHz photodiode. After this conversion, the electric waveform corresponds to the shape of the optical filtering function used in formation of the optical waveform.

The time window of the WSU is 3 ns; its width is determined by the optical bandwidth and the length of the optical expander. The resulting bandwidth of the RF signal is approximately 11 GHz. The analyzed system ensures formation of various waveforms, includ- ing ultra-wideband pulses, chirp-sinusoidal signals, and monocycles.

4.2. Compensation of Phase Distortion in Horn Antennas

At the first stage of studies of the antenna line transmitting USPs, its pulsed response $h(t) = U_{\text{rad}}(t)$ was measured. In these measurements, the radiating horn was fed with a 18-ps electromagnetic pulse obtained directly at the laser output and transmitted through a photodiode. The oscillogram of the signal at the output of the receiving horn is shown in Fig. 16. It is seen that the short pulse is dispersed and oscillations continuing four nanoseconds are clearly seen in the
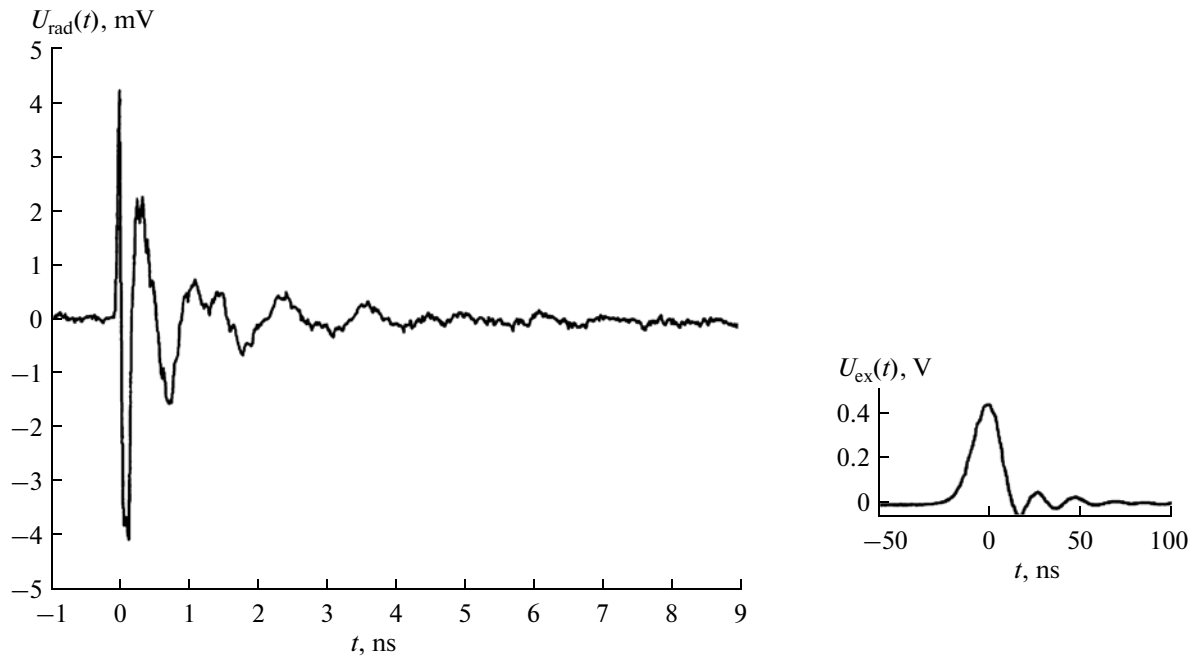
Fig. 16. Pulsed response of the antenna transmission line. The excitation pulse is shown in the inset.

received waveform. The received waveform has signs of a chirp signal with low-frequency components located near the boundary of the antenna passband (~900 MHz). Strong dispersion in the frequency band 0.9–14 GHz is a typical sign of substantial variations in the RF PFC.

Since the bandwidth of the input pulse (the inset in Fig. 16) is 27 GHz, which is much wider than the bandwidth of the antenna line (12 GHz), the received signal can be considered as a pulsed response. Using the data of the Fourier-transform of this pulsed response, we can determine the additional phase-frequency contribution of the pair of antennas. The sense of compensation of phase distortions is to compress the recorded waveform in time to a short pulse. This compression can be implemented if the phase of the input signal is the inverse of the phase created by the pair of antennas. It has been shown that the simplest optimized waveform ($x(t)$) reproducing the required pulse is the signal matched to the antenna transmission line, i.e., the time-reversed image of the pulsed response:

$$x(t) = h(-t). \tag{4}$$

In this case, the amplitude of the received voltage at the output of the antenna transmission line is determined by means of autocorrelation of its pulsed response:

$$r(t) = h(t) * h(-t), \tag{5}$$

where the asterisk denotes the convolution operation. Expression (4) describes the so-called matched filtering solution for the optimum input waveform.

In order to obtain an approximation of the signal matched to the analyzed antenna system, a sampled image of its real response is created and used to form the time-reversed pulsed response. Exactly this response is used as the optical filtering function controlling the WSU. The resulting shape of the electric signal $U_{pulse}(t) = x(t) \approx h(-t)$ is shown in Fig. 17. It is seen that the duration of the practically matched input signal is approximately 3 ns, i.e., 75% of the duration of the pulsed response shown in Fig. 16. If the practi-
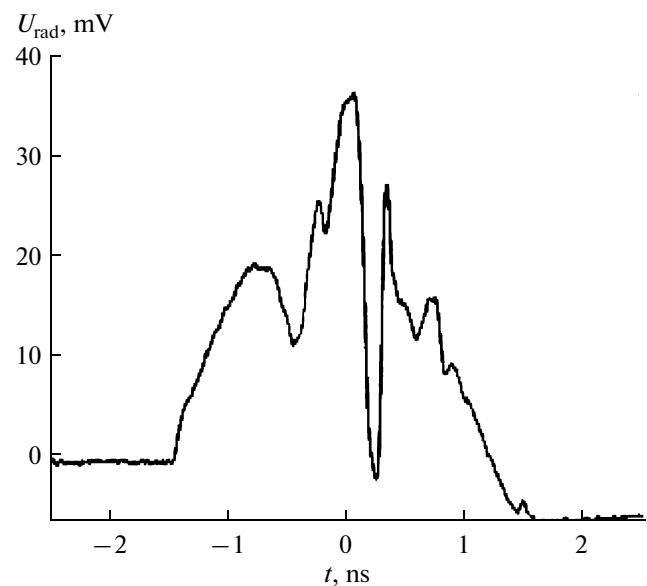

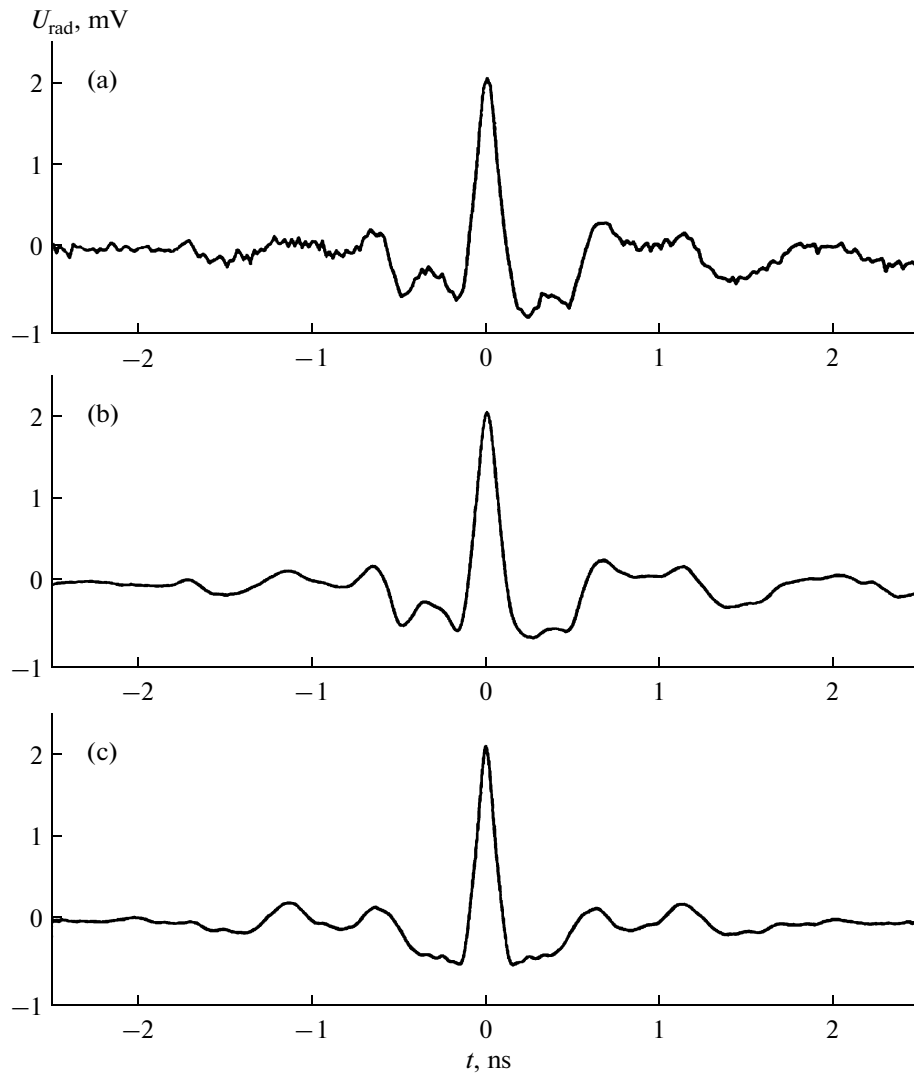**Fig. 17.** Practically matched input signal.

Fig. 18. Pulsed response of the antenna transmission line: (a) measured response in the case when the practically matched waveform is fed to the input, (b) calculated response in the case of excitation by the practically matched waveform, and (c) calculated response corresponding to excitation by the perfectly matched waveform.

cally matched signal is fed to the input of the radiating antenna, the waveform shown in Fig. 18a will be recorded at the output of the receiving antenna. The predicted (calculated) shape of response corresponding to this case is shown in Fig. 18b. It can readily be noticed that experimental and calculated data are very close. Indeed, comparison of the waveforms in Figs. 17, 18a, and 18b shows that excitation of the practically matched waveform causes strong compression of the pulse. The calculated shape of the pulsed response in the case of excitation of the antenna transmission line by the so-called perfectly matched waveform (5) is given in Fig. 18c. Qualitatively, all three curves shown in Figs. 18a–18c differ in only the relative sidelobe level, which is minimal in the case of perfect matching.

As follows from the aforesaid, small oscillations within 2 ns are caused by the following circumstance: the used shape of the practically matched signal covers only approximately 2 ns of the real pulsed response. Accordingly, low-frequency components existing beyond the 2-ns aperture are not "supplied" with phase compensation.

The efficiency of the considered compensation method is most evident when we compare corresponding pulsed intensities shown in Fig. 19. The curve in Fig. 19a corresponds to the intensity distribution of the measured pulsed response (Fig. 16), the curve in Fig. 19b is the intensity of the system response to the practically matched waveform, and the curve in Fig. 19c is the intensity of the response to the perfectly matched waveform. In two last cases, the response of

the antenna line is a monopulse and the pulse duration is substantially decreased.

5. MASTER CONTROLLER BASED ON FIBER-OPTIC BRAGG DIFFRACTION GRATINGS

A type of the fiber-optic pattern shaper that can simultaneously form a large number of independent beams in a wideband PAA was considered in [13, 14]. In this shaper, main elements forming controlled time delays are FO diffraction gratings (FODGs) and arrays of photodetectors. The topology of the considered controller contains a multiwave FODG distributed along the length of the optical fiber. The FODG is a section of single-mode optical guide whose core contains a formed and fixed structure with a refractive index periodically varying along the axis (Fig. 20) [15]. If a sufficiently wide spectrum of wavelengths propagates in this optical guide, each grating reflects backward radiation at only one wavelength. This effect is attained by means of appropriate selection of the grating period and the number of grating grooves. The package of gratings in Fig. 20 was designed for selection of N optical carriers. Since the gratings are separated by certain distances along the length of the optical guide, reflected optical components with different frequencies (wavelengths λ_i) have different phase delays.

The considered shaper uses multiwave Bragg gratings distributed along the length of the optical fiber and diffraction gratings with a linearly varying constant. The grating of the second type was used to implement a wide range of time delays in real time, which is required for phase equalization in multipattern PAAs. Such architecture substantially lowers the complexity of the PAA hardware, including the number of interconnections. This feature opens up possibilities for the design of large arrays with numbers of partial channels of 500−1000. Moreover, application of photodetectors at each beam port of the array of photodetectors eliminates the influence of the interference.

The functional block diagram of the pattern shaper is shown in Fig. 21. The profile of the time delays that the shaper must reproduce in order to equalize the pattern for one direction and attain the most efficient summation of fields is linear (Fig. 22). The analyzed design uses the partitioning concept according to which the array is divided into E groups with P elements in each group. This concept is reflected in Figs. 21 and 22.

Antenna elements can be created with the use of P equispaced optical wavelengths, which are the same for each group. This ensures the possibility of formation of the delay profile shown in Fig. 22. According to Fig. 22, each group of P elements is characterized by two components. One component is the slope angle of the profile of phase delays, which is called reference
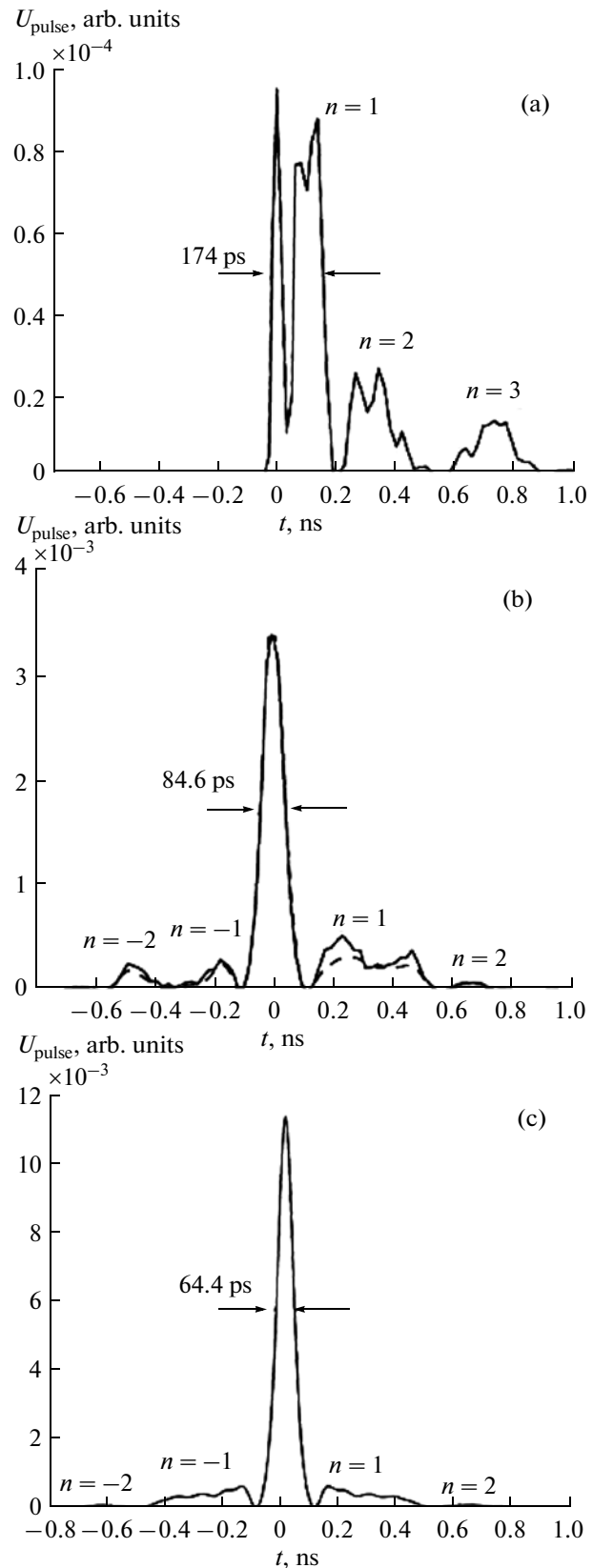

Fig. 19. Power density distributions of (a) the pulsed response of the antenna transmission line, (b) the system response to the practically matched waveform fed to the input, and (c) the calculated system response in the case of excitation by the perfectly matched waveform.
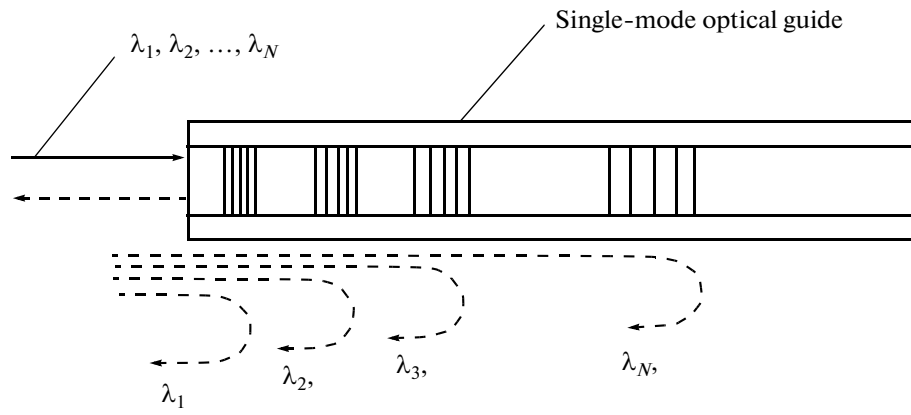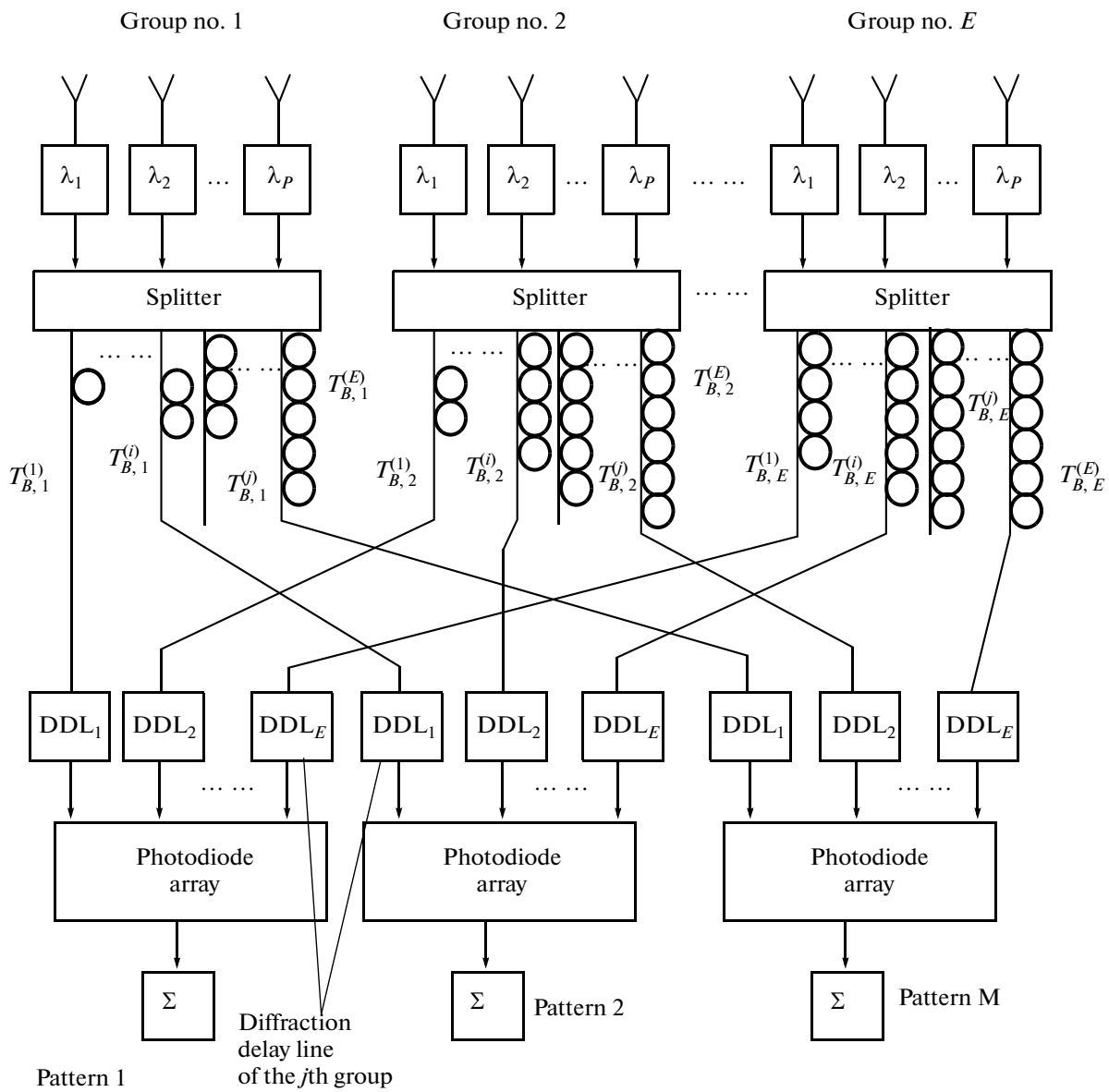
Fig. 20. Fiber-optic Bragg diffraction gratings.

Fig. 21. Functional block diagram of the shaper based on fiber-optic Bragg diffraction gratings.
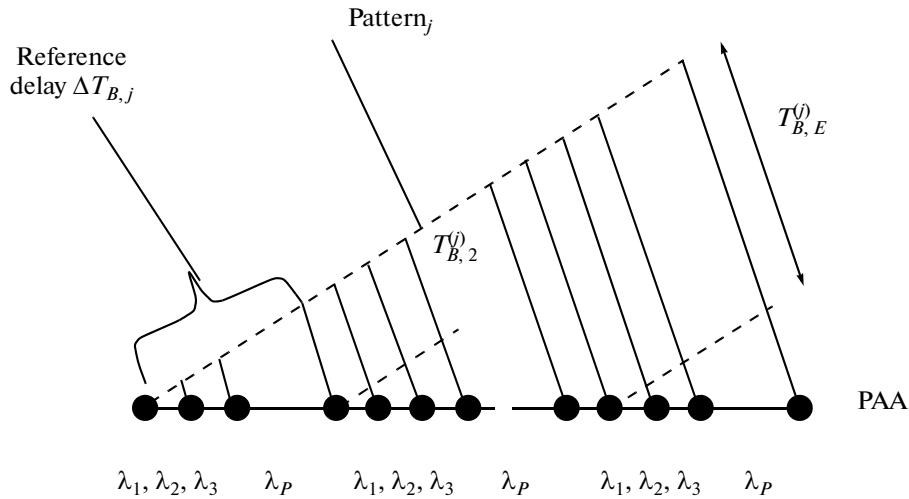
Fig. 22. Profile of the time delays required for phase equalization in one of pattern ports (*j*).

delay $\Delta T_{B,j}$ and is the same for all groups. The second component is the constant shift of delays, which is the same for all elements of a particular group $T_{B,E}^{(j)}$ but is different for different groups. Constant components of the delay are formed by standard FO guides by selecting their lengths so as to ensure the required values of parameters $T_{B,2-E}^{(j)}$ in a particular group. Reference delays $\Delta T_{B,j}$ are varied according to a linear time-frequency law are implemented by using periodically placed discrete Bragg gratings or diffraction gratings in a fiber with linearly varying refractive index. Hence, different wavelengths are reflected at different points along the fiber length; in this case, the required shape of the time-delay characteristic is attained. The considered shaping algorithm can also be used for all other directions of the array pattern. Radial $P : M$ splitters are used to split the optical signal of each group into M parts. Thus, in order to implement the M-pattern operating mode, M different patterns can be independently synthesized.

Each pattern port (Fig. 21) of the pattern shaper contains an array of photodetectors. At the output of this array, the sum signal of microwave subcarriers is extracted. As a result, for an M-element array, each photodetector detects only P wavelengths instead of N wavelengths. This is an important advantage of the proposed pattern shaper, which eliminates a serious problem associated with the interference noise.

6. COMPONENTS OF MODERN UWB RADARS WITH OPTOELECTRONIC CONTROL

Modern trends in the design and development of UWB and USP radars gave rise to the development of components used for the design of main functional units of these systems. This is primarily true for optoelectronic and fiber-optic components. Let us men-

tion literary sources describing advanced designs of antenna radiators [16−19], lasers [20], and semiconductor wideband amplifiers [21−23] operating in the frequency band 1−18 GHz.

Wideband optoelectronic phase shifters [24, 25] form a new type of devices for microwave circuit technology.

Specific features of the USP radar require application of special waveforms, which are matched to the receiving and transmitting antennas. Such waveforms can be created in real time with the help of modern high-speed optical Fourier spectrum analyzers and programmable waveform synthesizers. Key components of such devices are parametric microwave mixers [26] and fast gating devices [27].

Fiber-Optic Dispersing Prisms

At first stages of the studies on the development of optoelectronic controllers [3, 4], FODPs were manufactured from standard single-mode optical guides, for example, a fiber produced by Corning Inc., which has the group dispersion (GD) index $D = 88$ ps/(nm km). Here, the length of such fiber sections used in the FODP for a scanning interval of $\pm 30°$ is several hundred meters. In recent years, a manufacturing technique of the so-called photonic-crystal fibers (FCFs), which has substantially larger GD indices, has been developed. For example, the results of studies in which FCFs with the GD index $D > 500$ ps/(nm km) in the spectral band 1560−1580 nm were described in [28−30]. Further advances in the manufacturing technique gave rise to development of a FCF with even larger GD index ($D = 4000$ ps/(nm km)) [31]. Function $D(\lambda)$ of such FCFs is shown in Fig. 23. It is seen that, in the spectral band 1540−1550 nm, the GD index $|D| = 4000$ ps/(nm km). Thus, by applying modern FCFs, it is possible to decrease the length of FODP fiber sec-
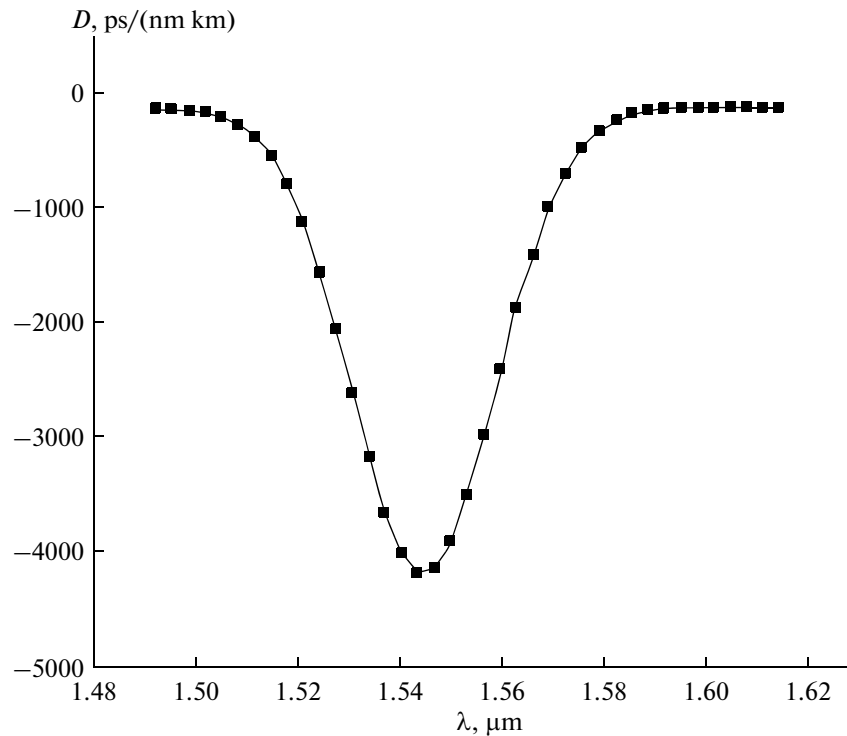
Fig. 23. Group dispersion of the photonic-crystal fiber [31].

tions more than 40 times, i.e., reduce the maximum length of the fiber section to 1.5–2 m.

Fiber-optic [32] or semiconductor [33] lasers can serve as light sources in the considered controller. These devices have a wavelength tuning range of more than 50 nm for a generation wavelength of 1500 nm; their output power is 0.1–1.0 mW.

As an the amplifier of the optical radiation in this wave band, it is expedient to use an EAU-350 erbium amplifier whose maximum gain is 35 dB and the maximum power is ~350 mW. Two types of electrooptical modulators, absorption modulators using the Stark effect and traveling-wave modulators based of the Mach−Zehnder interferometer, can be used. Absorption modulators on the basis of InGaAs and InAlAs films [34, 35] ensure modulation in a frequency band of up to 40 GHz at a control voltage of 5 V.

Traveling-wave modulators [36, 37] are manufactured on a $LiNbO_3$ single-crystal substrate with electrodes of a two-wire line located on the upper side of this substrate. In these modulators, the half-wave voltage corresponding to the 100-% modulation depth is 1–2 V.

A broad spectrum of semiconductor photodiodes, which are used for extraction of the microwave subcarrier, has been developed and is currently produced. For the considered spectral band, an EPD-1300-0-05

photodiode (produced by Epigap Optoelectronik GmbH) is most suitable. It has the following characteristics: the supply voltage is 5 V, the slope of the wolt−ampere characteristic $S = 0.9$ A/W, and the equivalent noise power is 1.1×10^{-14} W/Hz$^{-1/2}$.

CONCLUSIONS

Modern architectural design principles based on application of photonics methods are very promising for the development of UWB and USP radars. In the UWB radars of modern architecture, the PAA pattern is formed and controlled by high-speed photoelectronic controllers. Important advantages of these controllers consist in unification of their functional units and the possibility of application of integrated optical technologies for manufacturing the arrays of semiconductor lasers, electrooptical modulators, photodetectors, phase shifters, and integrated packages of wideband microwave amplifiers. Special photoelectronic controllers can be used for the real-time synthesis of required waveforms of radiated pulsed signals, matched to the receiving and transmitting antennas, which excludes dispersion spreading of the pulse. The effect of photoinduced microwave radiation generated by special doped films radiated by high-power optical pulses can be used to develop a compact feed of reflector antennas.

REFERENCES

1. L. D. Bakhrakh and A. A. Bliskavitskii, Antenny, No. 36, 4 (1989).
2. I. Frigyes and A. J. Seeds, IEEE Trans. Microwave Theory Tech. **43**, 2378 (1995).
3. M. Y. Frankel, P. J. Matthews, and R. D. Esman, IEEE Trans. Microwave Theory Tech. **44**, 2696 (1996).
4. M. Y. Frankel and R. D. Esman, IEEE Trans. Microwave Theory Tech. **43**, 2387 (1995).
5. M. Y. Frankel, P. J. Matthews, and R. D. Esman, IEEE Trans. Microwave Theory Tech. **45**, 1522 (1997).
6. D. W. Liu, J. B. Thaxter, and D. F. Bliss, Opt. Lett. **20**, 1444 (1995).
7. B. B. Hu, J. T. Darrow, X. C. Zhang, et al., Appl. Phys. Lett. **56**, 886 (1990).
8. N. A. Riza, IEEE Trans. Microwave Theory Tech. **45**, 1508 (1997).
9. N. A. Riza, Appl. Opt. **33**, 3712 (1994).
10. D. M. Pozar, IEEE Trans. Antennas Propag. **51**, 2335 (2003).
11. J. D. McKinney and A. M. Weiner, IEEE Trans. Microwave Theory Tech. **54**, 1681 (2006).
12. J. Chou, Y. Han, and B. Jalali, IEEE Photon. Technol. Lett. **15**, 581 (2003).
13. R. A. Minasian, IEEE Trans. Microwave Theory Tech. **54**, 832 (2006).
14. R. A. Minasian and K. E. Alameh, IEEE Trans. Microwave Theory Tech. **45**, 1513 (1997).
15. S. A. Vasil'ev, O. I. Medvedkov, I. G. Korolev, et al., Kvantovaya Elektron. (Moscow) **35**, 1085 (2005).
16. C. Ying and Y. P. Zhang, IEEE Trans. Antennas Propag. **53**, 3089 (2005).
17. R. Behdad and K. Sarabandi, IEEE Trans. Antennas Propag. **53**, 2185 (2005).
18. K. H. Kim and J. U. Kim, IEEE Trans. Antennas Propag. **53**, 3403 (2005).
19. H. Steyskal, J. Ramprecht, and H. Holter, IEEE Trans. Antennas Propag. **53**, 2558 (2005).
20. N. Dagli, IEEE Trans. Microwave Theory Tech. **47**, 1151 (1999).
21. S. Banba and H. Ogawa, IEEE Trans. Microwave Theory Tech. **43**, 485 (1995).
22. Y. Park, C. H. Lee, J. D. Cressler, and J. Laskar, IEEE Trans. Microwave Theory Tech. **54**, 1687 (2006).
23. N. J. Kolias and R. C. Compton, IEEE Trans. Microwave Theory Tech. **45**, 1204 (1997).
24. G. R. Lin, T. S. Hwang, J. H. Chuang, et al., IEEE Trans. Microwave Theory Tech. **46**, 1419 (1998).
25. F. V. Minnaar, J. C. Coetzee, and J. Joubert, IEEE Trans. Microwave Theory Tech. **45**, 1249 (1997).
26. A. Paolella, S. Malone, T. Barceli, and P. R. Herczfeld, IEEE Trans. Microwave Theory Tech. **43**, 518 (1995).
27. S. L. Huang, C. H. Lee, and H. A. Hung, IEEE Trans. Microwave Theory Tech. **43**, 1281 (1995).
28. L. P. Shen, W.-P. Huang, G. X. Chen, and S. S. Jian, IEEE Photon. Technol. Lett. **15**, 540 (2003).
29. J. A. West, N. Venkataraman, C. M. Smith, et al., in *Proc. 27th Eur. Conf. on Opt. Commun. (ECOC'01), Amsterdam, 30 Sept.—4 Oct. 2001* (IEEE, New York, 2001), Vol. 4, 582.
30. Y. Jiang, Z. Shi, B. Howley, et al., IEEE Photon. Technol. Lett. **17**, 187 (2005).
31. V. Gerome, J.-L. Auguste, and J.-M. Blondy, Opt. Lett. **29**, 2725 (2004).
32. D. G. Cooper, J. L. Dexter, and R. D. Esman, IEEE J. Select Topics Quantum Electronics **1** (1), 14 (1995).
33. H. Zmuda and E. N. Toughlian, *Photonic Aspects of Modern Radar* (Artech House, Norwood, 1994).
34. T. Ido, H. Sano, D. J. Moss, et al., IEEE Photon. Technol. Lett. **6**, 1207 (1994).
35. T. Ido, H. Sano, S. Tanaka, et al., J. Lightwave Technol. **14**, 2324 (1996).
36. G. K. Gopalakrishnan, W. K. Burns, R. W. McElhanon, et al., J. Lightwave Technol. **12**, 1807 (1994).
37. X. Zhang and T. Miyoshi, IEEE Trans. Microwave Theory Tech. **43**, 523 (1995).

Translated by A. Kondrat'ev